



Article

Thermoelectric Properties of Hexagonal M_2C_3 ($M = As, Sb, \text{ and } Bi$) Monolayers from First-Principles Calculations

Xue-Liang Zhu ¹, Peng-Fei Liu ² , Guofeng Xie ^{1,3,4,*}, Wu-Xing Zhou ^{3,4}, Bao-Tian Wang ² and Gang Zhang ^{5,*}

¹ School of Physics and Optoelectronics, Xiangtan University, Hunan 411105, China; zhuxl@ihep.ac.cn

² Institute of High Energy Physics, Chinese Academy of Sciences (CAS), Beijing 100049, China; pfliu@ihep.ac.cn (P.-F.L.); wangbt@ihep.ac.cn (B.-T.W.)

³ School of Materials Science and Engineering, Hunan University of Science and Technology, Xiangtan 411201, China; wuxingzhou@hnu.edu.cn

⁴ Hunan Provincial Key Laboratory of Advanced Materials for New Energy Storage and Conversion, Xiangtan 411201, China

⁵ Institute of High Performance Computing, Singapore 138632, Singapore

* Correspondence: gfxie@xtu.edu.cn (G.X.); zhangg@ihpc.a-star.edu.sg (G.Z.)

Received: 20 March 2019; Accepted: 5 April 2019; Published: 11 April 2019



Abstract: Hexagonal M_2C_3 compound is a new predicted functional material with desirable band gaps, a large optical absorption coefficient, and ultrahigh carrier mobility, implying its potential applications in photoelectricity and thermoelectric (TE) devices. Based on density-functional theory and Boltzmann transport equation, we systematically research the TE properties of M_2C_3 . Results indicate that the Bi_2C_3 possesses low phonon group velocity (~ 2.07 km/s), low optical modes (~ 2.12 THz), large Grüneisen parameters (~ 4.46), and short phonon relaxation time. Based on these intrinsic properties, heat transport ability will be immensely restrained and therefore lead to a low thermal conductivity (~ 4.31 W/mK) for the Bi_2C_3 at 300 K. A twofold degeneracy is observed at conduction bands along Γ -M direction, which gives a high n-type electrical conductivity. Its low thermal conductivity and high Seebeck coefficient lead to an excellent TE response. The maximum thermoelectric figure of merit (ZT) of n-type can approach 1.41 for Bi_2C_3 . This work shows a perspective for applications of TE and stimulate further experimental synthesis.

Keywords: M_2C_3 ; thermal conductivity; Seebeck coefficient; thermoelectric figure of merit

1. Introduction

Thermoelectric (TE) technology can directly convert heat energy into electrical power, playing an important role in solving current energy and environmental crises [1–3]. However, low conversion efficiency and high cost are currently facing two crucial bottlenecks [4]. Generally, the conversion efficiency of a TE material is evaluated in terms of a dimensionless thermoelectric figure of merit (ZT) [5–7],

$$ZT = \frac{S^2 \sigma T}{\kappa} \quad (1)$$

where S , σ , and T are the Seebeck coefficient, electrical conductivity, and absolute temperature. κ is the thermal conductivity, which is composed of the lattice thermal conductivity κ_l and electronic thermal conductivity κ_e . However, optimizing one parameter without affecting another is difficult due to the complex competition [8]. The common measures to enhance TE performance mainly concentrate on regulating electrical transport coefficients by band-structure engineering [9] and/or suppressing

the heat conductivity ability through nanostructuring [10]. These methods are benefits to simplify conflicting parameters, and further enhance the TE performance.

Since exfoliating graphene from graphite by the mechanical cleavage method in 2004 [11], researching two-dimensional (2D) functional materials has recently drawn much attention in materials science [12–17]. Unfortunately, graphene is unsuitable for TE materials because of its small band gap and ultrahigh κ_l [18]. The most common pristine TE materials are IV–VI (PbTe [19], Bi₂Te₃ [20], PbSe [21],) compounds, all of which possess a fairly low thermal conductivity. Generally, these TE materials contain heavy atoms with a relatively narrow band gap, because heavy atoms give rise to low lattice vibrational frequency that results in a low κ_l [22]. For example, SnSe has been found to show high TE performance ($ZT \sim 2.6$ at 300 K) and inherently low thermal conductivity (~ 0.25 W/mK) [23]. The intrinsic thermal transport property in SnSe mainly attributes to its strong anharmonic effect [24]. With the extraordinary electrical transport properties, the SnSe really surprises the field of science as a hopeful TE material. Therefore, we should research the TE properties of new functional materials.

Very recently, a new IV–VI compounds, M₂C₃ (M = As, Sb, and Bi), which could be synthesized by appropriate substrates, has been successfully predicted [25]. It is reported that the As₂C₃ has an ultrahigh electron mobility of 4.45×10^5 cm²V⁻¹s⁻¹, which is significantly higher than that of the MoS₂ (~ 200 cm²V⁻¹s⁻¹) [26]. Meanwhile, compared with the other 2D materials, such as phosphorus [27], boron nitride [28], and silicene [29], it exhibits desirable band edge locations and a large optical absorption coefficient. These outstanding properties suggest M₂C₃ monolayers could be hopeful functional materials for next-generation high-performance devices. In this work, we systematically study the TE properties of the M₂C₃ monolayers by using Boltzmann transport theory. The κ_l is computed by utilizing the self-consistent iterative approach. Results indicate that the intrinsic low κ_l is 20.82, 9.35, and 4.31 W/mK for As₂C₃, Sb₂C₃, and Bi₂C₃ at room temperature, respectively. Detailed discussions of phonon scattering curves, phonon velocities, phonon relaxation time, and Grüneisen parameters are exhibited to explain its low κ_l . A high Seebeck coefficient can be observed in electrical transport. The maximum ZT can approach 0.93, 1.17, and 1.41 for the As₂C₃, Sb₂C₃, and Bi₂C₃ at 700 K, respectively. Calculated results shed light on the idea that the M₂C₃ is a hopeful candidate for TE applications.

2. Methods

In this paper, the M₂C₃ is calculated by utilizing the Vienna ab initio simulation package (VASP) [30] within the framework of the Perdew–Burke–Ernzerhof (PBE) [31] generalized gradient approximation [32]. A $9 \times 9 \times 1$ *k*-mesh and kinetic energy cutoff of 500 eV were used for structure optimization in the Brillouin zone (BZ). A vacuum layer of 20 Å thickness along the *z* direction was employed to eliminate interlayer interactions. All crystal structures were fully optimized until the total energy variation was less than 10^{-6} eV/Å, and the residual forces atoms were less than 0.01 eV/Å. In order to accurately evaluate electronic structure, the Heyd–Scuseria–Ernzerhof (HES06) hybrid density functional was adopted [33]. The electrical transport properties were obtained by semiclassical Boltzmann transport theory as implemented in the BoltzTraP code [34]. This method has successfully predicted many TE materials [35,36]. A dense $45 \times 45 \times 1$ *k*-mesh was used in the BZ.

Using the ShengBTE code [37], the phonon transport properties were calculated from the Boltzmann transport equation, in which the harmonic second-order interaction force constants (2nd IFCs) and the anharmonic third-order IFCs (3rd IFCs) were used as input. The phonon dispersions and 2nd IFCs were calculated by utilizing PHONOPY packages [38]. A $2 \times 2 \times 1$ supercell with $3 \times 3 \times 1$ *k*-mesh was used. The anharmonic 3rd IFCs were obtained by using the $2 \times 2 \times 1$ supercell with the finite-difference method [39]. The interactions including the sixth-nearest-neighbor atoms were taken into account for the 3rd IFCs. Based on the test of *k*-mesh, a dense $35 \times 35 \times 1$ *k*-mesh was used to calculate κ_l .

3. Results and Analysis

3.1. Atomic and Electronic Structures

As illustrated in Figure 1a,b the monolayer M_2C_3 is a hexagonal crystal system with high space group $P6/mmm$ (No. 191). The optimized lattice constant is 5.86, 6.39, and 6.70 Å for As_2C_3 , Sb_2C_3 , and Bi_2C_3 , which is excellently consistent with a previous theoretical prediction [25]. There are four M (M = As, Sb, and Bi) atoms and six C atoms in the primitive cell. Interestingly, it looks like an enlarging of arsenene [40] with the insertion into a 2D mesh of C atoms from a top view. From the side, the monolayer M_2C_3 possesses puckered configuration. As shown in Table 1, the interatomic distance of M-C shows a lengthening trend, resulting in the enhancement of atomic vibration frequency. More details are summarized in Table 1.

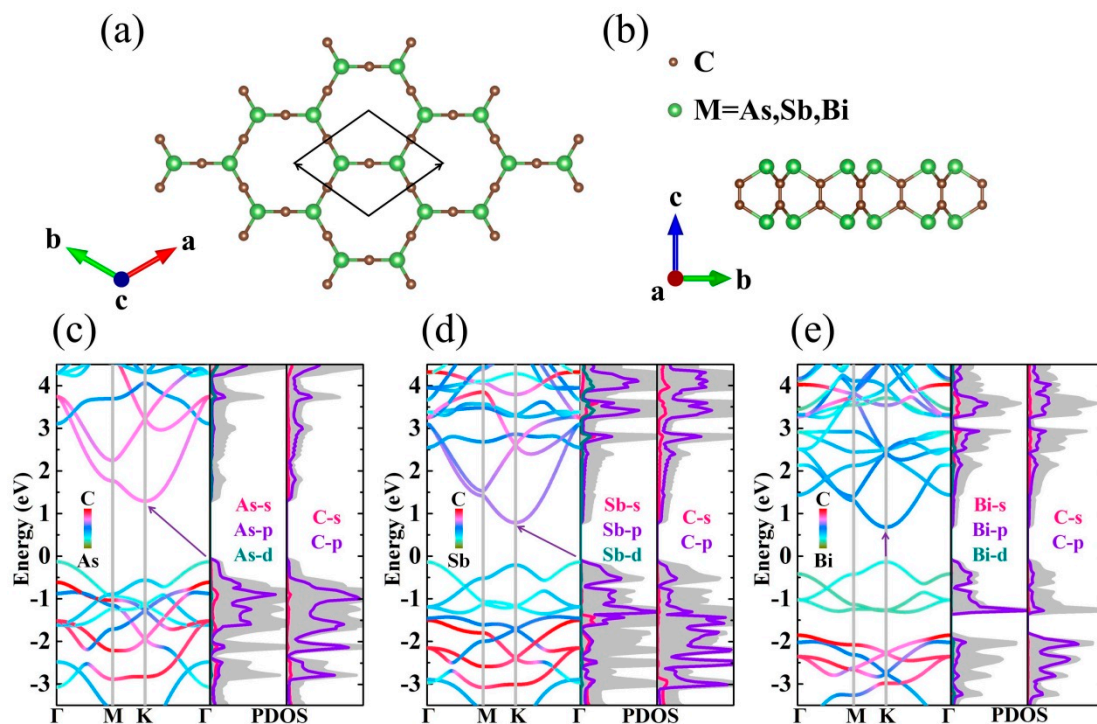


Figure 1. Top (a) and side (b) view for monolayer M_2C_3 . The band structures and corresponding projected density of states (PDOS) for (c) As_2C_3 , (d) Sb_2C_3 , and (e) Bi_2C_3 .

Table 1. The lattice constants (l_a), bond lengths of C-C (l_{C-C}), bond lengths of M-C (l_{M-C}), and band gaps based on Perdew–Burke–Ernzerhof (PBE) and HES06.

Type	l_a (Å)	l_{C-C} (Å)	l_{M-C} (Å)	PBE (eV)	HES06 (eV)
As_2C_3	5.86	1.33	2.00	1.42	2.27
Sb_2C_3	6.39	1.33	2.20	0.92	1.53
Bi_2C_3	6.70	1.33	2.31	0.81	1.28

The band structures and corresponding projected density of states (PDOS) of monolayer M_2C_3 are shown in Figure 1. Obviously, As_2C_3 and Sb_2C_3 are indirect band gap semiconductors with the valence band maximum (VBM) and the conduction band minimum (CBM) located at the Γ and K points, respectively. Monolayer Bi_2C_3 exhibits a direct band gap of 0.81 eV, which is smaller than that of As_2C_3 (1.42 eV) and Sb_2C_3 (0.92 eV). Near the Fermi level, one can see that the bands primarily stem from the M-p orbitals. Interestingly, the two lowest conduction bands (CB) display overlap along Γ -M direction. A twofold degeneracy is observed in Sb_2C_3 and Bi_2C_3 , which gives rise to a high n-type electrical conductivity. The PDOS fully shows that the valence band (VB) and CB are mainly

occupied by the p orbitals. Remaining orbitals almost have no contribution around the Fermi level. Meanwhile, we also find that it exhibits stair-like PDOS, which can increase the Seebeck coefficient [41]. Therefore, an intrinsic CB degeneracy and a stair-like PDOS are obtained in monolayer M_2C_3 , which are considered to be the electronic transport characteristics of high performance TE devices [42].

3.2. Electrical Transport Properties

The S , σ , and κ_e are indispensable for analyzing the TE performance of monolayer M_2C_3 . The electrical transport properties are obtained by solving semiclassical Boltzmann transport equation [33,43] combining with a constant relaxation time approximation. Here, we further imitate the doping effects of electronic transport by using the rigid band approximation. Based on these methods, the shape of electronic band structure is assumed to be invariant under light doping, and only moves up or down at the Fermi level for n- and p-type doping, respectively [44,45]. The negative and positive μ equate to n- and p-type, respectively. Based on Boltzmann transport equation, the electrical transport coefficients as functions of chemical potential μ and temperature can be derived [33],

$$\sigma_{\alpha\beta}(T, \mu) = \frac{1}{V} \int \sum_{\alpha\beta}(\epsilon) \left[-\frac{\partial f_{\mu}(T, \epsilon)}{\partial \epsilon} \right] d\epsilon \quad (2)$$

$$S_{\alpha\beta}(T, \mu) = \frac{1}{eTV\sigma_{\alpha\beta}(T, \mu)} \int \sum_{\alpha\beta}(\epsilon)(\epsilon - \mu) \left[-\frac{\partial f_{\mu}(T, \epsilon)}{\partial \epsilon} \right] d\epsilon \quad (3)$$

where $\alpha\beta$ and V are Cartesian index and the volume of the primitive cell, and the electrical transport distribution function $\sum_{\alpha\beta}(\epsilon)$ is given by

$$\sum_{\alpha\beta}(\epsilon) = \frac{e^2}{N_0} \sum_{i, \mathbf{q}} \tau v_{\alpha}(i, \mathbf{q}) v_{\beta}(i, \mathbf{q}) \frac{\delta(\epsilon - \epsilon_{i, \mathbf{q}})}{d\epsilon} \quad (4)$$

where N_0 , i , τ , and v are the sum of \mathbf{q} points, the band index, the electron relaxation time, and the electron group velocity.

Figure 2a–c shows the Seebeck coefficients for monolayer M_2C_3 . Obviously, the temperature-dependent decreasing behavior of the Seebeck coefficients is slowing down along with increasing the temperature. Surprisingly, the monolayer As_2C_3 has a very high Seebeck coefficient of 2.27 mV/K, which is visibly higher than that of Sb_2C_3 (1.37 mV/K) and Bi_2C_3 (1.31 mV/K) at room temperature. Compared with some high-performance TE materials ($PbTe$ [19], $SnSe$ [23], Bi_2O_2Se [46]), the monolayer M_2C_3 exhibits an ultrahigh Seebeck coefficient. These high Seebeck coefficients mainly originate from energy-dependent PDOS as shown in Figure 1. For a doped semiconductor, the Seebeck coefficient can be given by [47],

$$S = \frac{\pi^2 k_B^2 T}{3e} \left\{ \frac{1}{n} \frac{dn(\epsilon)}{d\epsilon} + \frac{1}{\mu} \frac{d\mu(\epsilon)}{d\epsilon} \right\}_{\epsilon=\mu} \quad (5)$$

where k_B is the Boltzmann constant. Equation (5) implies that the stair-like PDOS contains several sharp peaks, which can enhance carrier concentration $n(\epsilon)$ and give a high Seebeck coefficient.

The electrical conductivity with respect to scattering time σ/τ is presented in Figure 2d–f. Unlike the Seebeck coefficient, the maximum σ/τ for As_2C_3 is lower than that of Sb_2C_3 and Bi_2C_3 . Meanwhile, it is found that no matter what kind of materials, the σ/τ of n-type is always higher than that of the p-type, which is mainly attributed to the PDOS. We can see clearly that the slope of σ/τ will be flattened in low μ region (−0.5–0.5 eV) with the temperature increasing. The κ_e with respect to the relaxation time is shown in Figure 2g–i via the Wiedemann–Franz law [48]

$$\kappa_e = L\sigma T \quad (6)$$

where $L = \pi^2 \kappa_B^2 / 3e^2$ is the Lorenz number. Similar to the σ/τ , the κ_e/τ displays analogous curves. The κ_e/τ gradually increases along with varying the absolute value of the μ from the Fermi energy level ($\mu = 0$). These transport coefficients indicate that the monolayer M_2C_3 has a good performance of electronic transport ability with n-type.

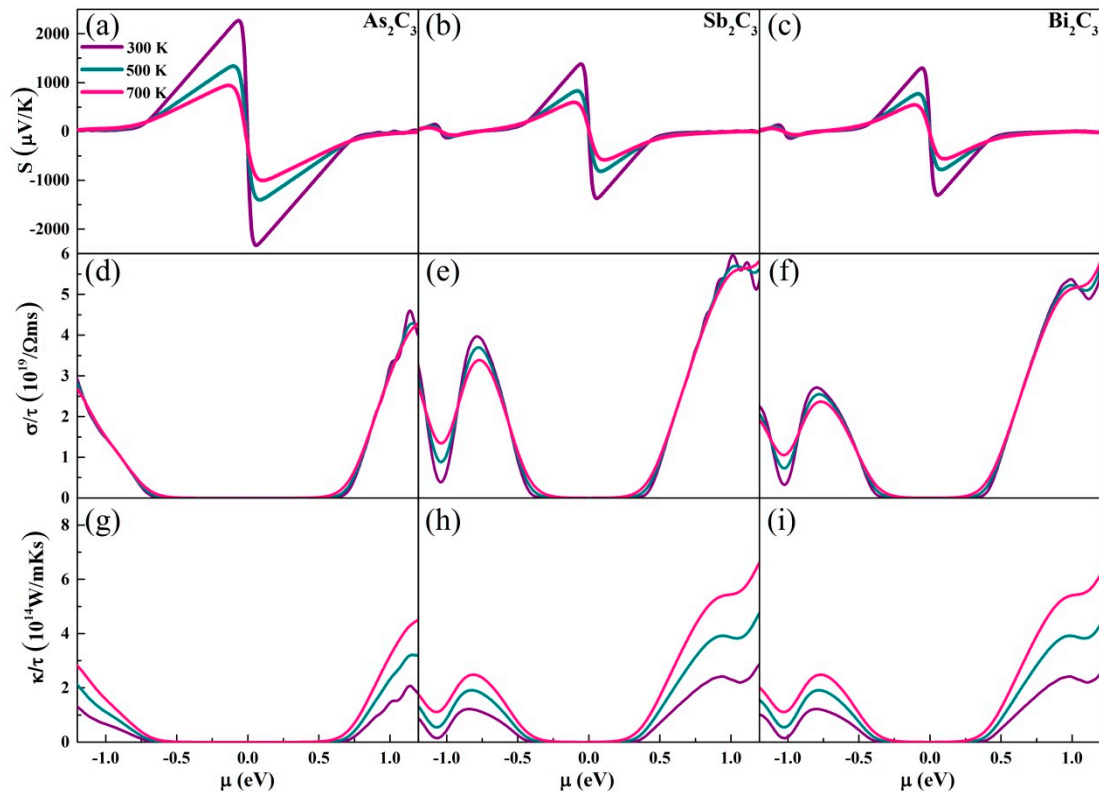


Figure 2. (a–c) Seebeck coefficients, (d–f) electrical conductivity, and (g–i) electronic thermal conductivity with respect to the scattering time at different temperatures.

3.3. Phonon Transport Properties

The phonon scattering curves of monolayer M_2C_3 is shown in Figure 3. No imaginary phonon frequencies appear in the phonon spectra, which indicates that the monolayer M_2C_3 is thermodynamically stable at ambient pressure. The acoustic branches of M_2C_3 exhibit a common phenomenon in 2D systems with a parabolic dispersion of out-of-plane acoustic mode and two linear dispersions of in-plane modes at the Γ point [49]. As shown in Figure 3, one can see that the M atoms dominate the low frequency region (below ~ 10 THz), while the remaining area is from the C atomic contributions. Meanwhile, we also find that the acoustic modes for As_2C_3 , Sb_2C_3 , and Bi_2C_3 exhibit a downward moving trend, which can be attributed to the larger of atomic mass. It is noted that the low frequency optical modes are alternating and softening with the three acoustic branches for the monolayer M_2C_3 , resulting in strong acoustic–optical interactions. This is similar to the PbSe [50], which has strong anharmonic effects. The boundary frequency of lowest optical branch displays a decreasing trend with the following order: As_2C_3 (4.18 THz) > Sb_2C_3 (3.08 THz) > Bi_2C_3 (2.12 THz). To further analyze phonon scattering properties, the corresponding phonon density of states (PhDOS) is presented. From the PhDOS, we can see clearly that the acoustic phonon branches mainly contain the M vibrations, while the contributions from C (xy) vibrations are mainly limited to 10 to 25 THz. The high frequency region from 45 to 50 THz is fully occupied by C (z) vibrations. In addition, the PhDOS also shows several peaks especially in optical branches region, which can give rise to the small phonon group velocity.

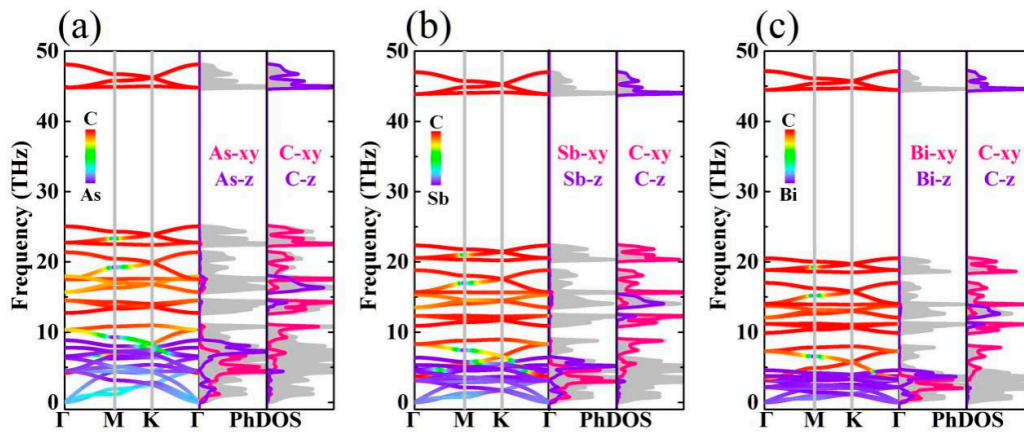


Figure 3. The orbital-resolved phonon spectra and corresponding phonon density of states (PhDOS) for (a) As_2C_3 , (b) Sb_2C_3 , and (c) Bi_2C_3 .

Based upon the phonon kinetic theory, the κ_l can be calculated as below:

$$\kappa_{l,\alpha\beta} = \sum_{q\lambda} C_V(q\lambda) v^\alpha(q\lambda) v^\beta(q\lambda) \tau_{q\lambda} \quad (7)$$

where C_V , v^α is the phonon specific heat and the phonon group velocity along α direction, and $\tau_{q\lambda}$ is the phonon relaxation time for the phonon mode λ at the wave vector \mathbf{q} . The κ_l of monolayer M_2C_3 , at temperatures from 300 K to 800 K, are plotted in Figure 4a. Obviously, the intrinsic κ_l shows evident temperature dependence, proportional to the inverse of the temperature $1/T$. In the high temperature, this dependence behavior is deemed to a common phenomenon of crystals, which attribute to the intrinsic enhancement of phonon–phonon scattering. At room temperature, we can see clearly that the Bi_2C_3 exhibits an intrinsic low κ_l of 4.31 W/mK, which is lower than those of the Sb_2C_3 (9.53 W/mK) and As_2C_3 (20.82 W/mK). In general, the κ_l is mainly dominated by the acoustical modes for the monolayer systems [51]. Because the mass of Bi is larger than that of As and Sb, acoustical phonons have lower frequencies for Bi_2C_3 than for As_2C_3 and Sb_2C_3 . These acoustic modes with low frequency might cause the small phonon group velocities, leading to the low κ_l .

The phonon group velocities are the important indicator for the assessment of heat transport ability. Using the phonon dispersion, the phonon group velocities can be obtained by

$$v_\lambda(\mathbf{q}) = \frac{d\omega_\lambda(\mathbf{q})}{dq} \quad (8)$$

The corresponding group velocities are plotted in Figure 4b. Much large values of the group velocities can be observed in low frequency region, while the high frequency modes exhibit relatively small group velocities. Meanwhile, it can be seen clearly that the group velocities from large to small is monolayer $\text{As}_2\text{C}_3 > \text{Sb}_2\text{C}_3 > \text{Bi}_2\text{C}_3$, which is consistent with the above analysis. This phenomenon similar to the GeS and SnS [52], which may attribute to large atomic mass.

To identify the underlying mechanism of low κ_l , we introduce the Grüneisen parameters and phonon relaxation time as shown in Figure 4c,d. The Grüneisen parameter can fully reflect the anharmonic interactions of a crystal, which is essential for analyzing the intrinsic characteristics of κ_l . The Grüneisen parameter can be described by

$$\gamma_\lambda(\mathbf{q}) = -\frac{V}{\omega_\lambda(\mathbf{q})} \frac{\partial \omega_\lambda(\mathbf{q})}{\partial V}. \quad (9)$$

It is noted that the large Grüneisen parameters can be observed at a low frequency region. Usually, large Grüneisen parameters (absolute value) indicate strong anharmonicity, which can give rise to low

κ_l . The averages of the acoustic Grüneisen parameters (absolute value) are calculated to be 2.61, 4.25, and 4.46 for As_2C_3 , Sb_2C_3 , and Bi_2C_3 , respectively. Obviously, the Bi_2C_3 exhibits larger Grüneisen parameter than that of As_2C_3 and Sb_2C_3 , indicating that Bi_2C_3 possesses stronger anharmonicity. To further explore the thermal transport properties, we show the phonon relaxation time in Figure 4d. The phonon relaxation time of Bi_2C_3 is much shorter than that of the As_2C_3 and Sb_2C_3 at 300 K, which is a significant factor for the low κ_l of Bi_2C_3 . More phonon transport details are summarized in Table 2.

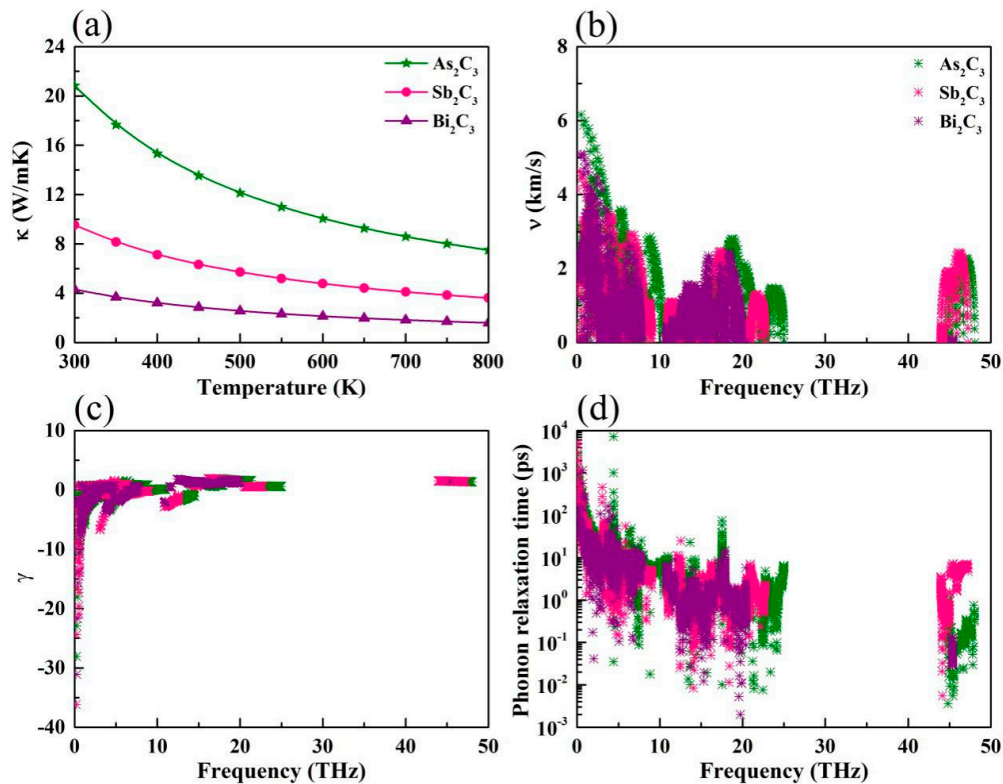


Figure 4. (a) Calculated lattice thermal conductivity of M_2C_3 versus temperature. (b) Phonon group velocity, (c) Grüneisen parameters, and (d) phonon relaxation time versus frequency for M_2C_3 , respectively.

Table 2. Summary of the lattice thermal conductivity κ_l (W/mK), the averages of the acoustic group velocity \bar{v} (km/s) and Grüneisen parameters $\bar{\gamma}$, and the lowest optical frequency ω_o (THz) for the As_2C_3 , Sb_2C_3 , and Bi_2C_3 , respectively.

Type	κ_l	\bar{v}	$\bar{\gamma}$	ω_o
As_2C_3	20.82	2.59	2.61	4.18
Sb_2C_3	9.53	2.15	4.25	3.08
Bi_2C_3	4.31	2.07	4.46	2.12

3.4. Thermoelectric Figure of Merit

Based on these transport coefficients, we estimate the ZT of M_2C_3 at three typical temperatures. The electronic relaxation time τ is employed from a previous report [25] and calculated by deformation potential theory [53]. The calculated ZT of M_2C_3 is presented in Figure 5. We can see that the two peaks move gradually towards the Fermi energy level ($\mu = 0$ eV), which originate from the decrease of band gap. Unlike the Seebeck coefficient, the ZT value has an enhancing behavior with the increasing temperature. Meanwhile, we can note that the ZT of n-type is always higher than that of the p-type for M_2C_3 , which mainly stems from their difference in electrical conductivity. In general, if the ZT value approach 1, it can be considered as a good TE material [54]. Due to the excellent transport

performance of electrons, the maximum ZT value can reach 0.93, 1.17, and 1.41 for As_2C_3 , Sb_2C_3 , and Bi_2C_3 , respectively.

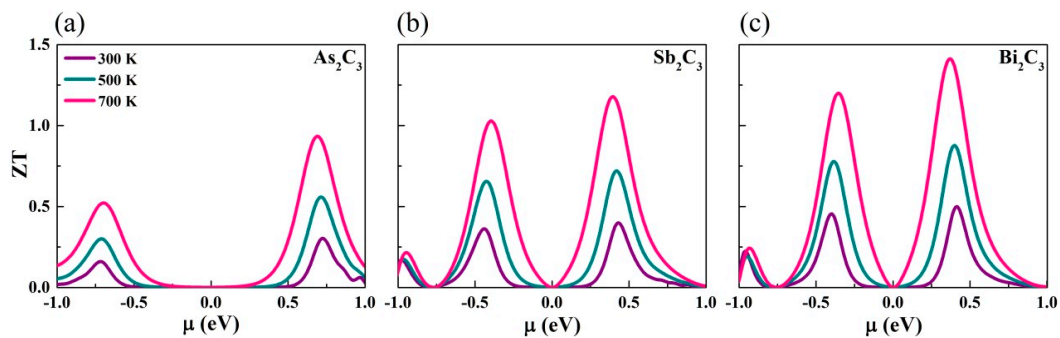


Figure 5. The thermoelectric figure of merit (ZT) versus the chemical potential of the (a) As_2C_3 , (b) Sb_2C_3 , and (c) Bi_2C_3 at different temperatures.

4. Conclusions

In summary, we report on the TE properties of monolayer M_2C_3 , through using the first-principles calculations and solving Boltzmann transport equation. The results indicate the monolayer M_2C_3 exhibits low κ_l at room temperature, especially for the Bi_2C_3 (~4.31 W/mK). Compared to most TE materials, the Bi_2C_3 exhibits analogous intrinsic properties, such as small group velocity, short relaxation time, and large Grüneisen parameters. A twofold degeneracy and stair-like PDOS are observed, which can lead to a high Seebeck coefficient. Finally, combining with available transport parameters, the ZT is found to be about 0.93, 1.17, and 1.41 for the As_2C_3 , Sb_2C_3 , and Bi_2C_3 at 700 K, respectively. This work indicates that the M_2C_3 is very promising for TE applications.

Author Contributions: Conceptualization, G.X. and G.Z.; Methodology, P.-F.L.; Software, X.-L.Z.; Validation, G.X., G.Z. and B.-T.W.; Formal Analysis, X.-L.Z.; Investigation, X.-L.Z.; Resources, X.-L.Z.; Data Curation, W.-X.Z.; Writing—Original Draft Preparation, X.-L.Z.; Writing—Review & Editing, G.X.; Visualization, X.-L.Z.; Supervision, B.-T.W.; Project Administration, G.X.; Funding Acquisition, G.X.

Funding: The calculations were performed at the Supercomputer Centre in the China Spallation Neutron Source. This work was financially supported by National Natural Science Foundation of China (NSFC) (Grant Nos. 11874145, 61604053) and the PhD Start-up Fund of Natural Science Foundation of Guangdong Province, China, (No. 2018A0303100013).

Conflicts of Interest: The authors declare no conflict of interest.

References

1. Chu, S.; Cui, Y.; Liu, N. The path towards sustainable energy. *Nat. Mater.* **2017**, *16*, 16–22. [[CrossRef](#)]
2. Aneke, M.; Wang, M. Energy storage technologies and real life applications—A state of the art review. *Appl. Energy* **2016**, *179*, 350–377. [[CrossRef](#)]
3. Wang, J.; Xie, F.; Cao, X.H.; An, S.C.; Zhou, W.X.; Tang, L.M.; Chen, K.Q. Excellent Thermoelectric Properties in monolayer WSe_2 Nanoribbons due to Ultralow Phonon Thermal Conductivity. *Sci. Rep.* **2017**, *7*, 41418. [[CrossRef](#)]
4. Ouyang, Y.; Zhang, Z.; Li, D.; Chen, J.; Zhang, G. Emerging Theory, Materials, and Screening Methods: New Opportunities for Promoting Thermoelectric Performance. *Ann. Phys.* **2019**. [[CrossRef](#)]
5. Zhang, X.; Zhao, L.D. Thermoelectric materials: Energy conversion between heat and electricity. *J. Materiomics* **2015**, *1*, 92–105. [[CrossRef](#)]
6. Zhao, L.D.; Dravid, V.P.; Kanatzidis, M.G. The panoscopic approach to high performance thermoelectrics. *Energy Environ. Sci.* **2014**, *7*, 251–268. [[CrossRef](#)]
7. Snyder, G.J.; Toberer, E.S. Complex thermoelectric materials. *Nat. Mater.* **2008**, *7*, 105–114. [[CrossRef](#)]
8. Heremans, J.P.; Jovovic, V.; Toberer, E.S.; Saramat, A.; Kurosaki, K.; Charoenphakdee, A.; Yamanaka, S.; Snyder, G.J. Enhancement of thermoelectric efficiency in PbTe by distortion of the electronic density of states. *Science* **2008**, *321*, 554–557. [[CrossRef](#)]

9. Pei, Y.; Wang, H.; Snyder, G.J. Band engineering of thermoelectric materials. *Adv. Mater.* **2012**, *24*, 6125. [[CrossRef](#)]
10. Kim, W. Strategies for engineering phonon transport in thermoelectrics. *J. Mater. Chem. C* **2015**, *3*, 10336–10348. [[CrossRef](#)]
11. Novoselov, K.S.; Geim, A.K.; Morozov, S.V.; Jiang, D.; Katsnelson, M.I.; Grigorieva, I.V.; Dubonos, S.V.; Firsov, A.A. Two-dimensional gas of massless Dirac fermions in graphene. *Nature* **2005**, *438*, 197–200. [[CrossRef](#)] [[PubMed](#)]
12. Xu, M.; Liang, T.; Shi, M.; Chen, H. Graphene-like two-dimensional materials. *Chem. Rev.* **2013**, *113*, 3766–3798. [[CrossRef](#)] [[PubMed](#)]
13. Wang, Q.H.; Kalantar-Zadeh, K.; Kis, A.; Coleman, J.N.; Strano, M.S. Electronics and optoelectronics of two-dimensional transition metal dichalcogenides. *Nat. Nanotechnol.* **2012**, *7*, 699–712. [[CrossRef](#)] [[PubMed](#)]
14. Zhang, W.B.; Qu, Q.; Zhu, P.; Lam, C.H. Robust intrinsic ferromagnetism and half semiconductivity in stable two-dimensional single-layer chromium trihalides. *J. Mater. Chem. C* **2015**, *3*, 12457–12468. [[CrossRef](#)]
15. Xie, G.F.; Ju, Z.F.; Zhou, K.K.; Wei, X.L.; Guo, Z.X.; Cai, Y.Q.; Zhang, G. Ultra-low thermal conductivity of two-dimensional phononic crystals in the incoherent regime. *npj Comput. Mater.* **2018**, *4*, 21. [[CrossRef](#)]
16. Chen, X.K.; Xie, Z.X.; Zhou, W.X.; Tang, L.M.; Chen, K.Q. Thermal rectification and negative differential thermal resistance behaviors in graphene/hexagonal boron nitride heterojunction. *Carbon* **2016**, *100*, 492–500. [[CrossRef](#)]
17. Tang, L.P.; Tang, L.M.; Geng, H.; Yi, Y.P.; Wei, Z.M.; Chen, K.Q.; Deng, H.X. Tuning transport performance in two-dimensional metal-organic framework semiconductors: Role of the metal d band. *Appl. Phys. Lett.* **2018**, *112*, 012101. [[CrossRef](#)]
18. Balandin, A.A.; Ghosh, S.; Bao, W.; Calizo, I.; Teweldebrhan, D.; Miao, F.; Lau, C.N. Superior thermal conductivity of single-layer graphene. *Nano Lett.* **2008**, *8*, 902–907. [[CrossRef](#)] [[PubMed](#)]
19. Yan, Q.; Chen, H.; Zhou, W.; Hng, H.H.; Boey, F.Y.C.; Ma, J. A simple chemical approach for PbTe nanowires with enhanced thermoelectric properties. *Chem. Mater.* **2008**, *20*, 6298–6300. [[CrossRef](#)]
20. Min, Y.; Roh, J.W.; Yang, H.; Park, M.; Kim, S.I.; Hwang, S.; Lee, S.M.; Lee, K.H.; Jeong, U. Surfactant-Free Scalable Synthesis of Bi₂Te₃ and Bi₂Se₃ Nanoflakes and Enhanced Thermoelectric Properties of Their Nanocomposites. *Adv. Mater.* **2013**, *25*, 1425–1429. [[CrossRef](#)]
21. Androulakis, J.; Lee, Y.; Todorov, I.; Chung, D.Y.; Kanatzidis, M. High-temperature thermoelectric properties of n-type PbSe doped with Ga, In, and Pb. *Phys. Rev. B* **2011**, *83*, 195209. [[CrossRef](#)]
22. Pal, K.; Anand, S.; Waghmare, U.V. Thermoelectric properties of materials with nontrivial electronic topolog. *J. Mater. Chem. C* **2015**, *3*, 12130–12139. [[CrossRef](#)]
23. Zhao, L.D.; Lo, S.H.; Zhang, Y.; Sun, H.; Tan, G.; Uher, C.; Wolverton, C.; Dravid, V.P.; Kanatzidis, M.G. Ultralow thermal conductivity and high thermoelectric figure of merit in SnSe crystals. *Nature* **2014**, *508*, 373–377. [[CrossRef](#)]
24. Delaire, O.; Ma, J.; Marty, K.; May, A.F.; McGuire, M.A.; Du, M.H.; Singh, D.J.; Ehlers, G.; Lumsden, M.D.; Sales, B.C. Giant anharmonic phonon scattering in PbTe. *Nat. Mater.* **2011**, *10*, 614–619. [[CrossRef](#)]
25. Liu, P.F.; Bo, T.; Liu, Z.; Eriksson, O.; Wang, F.; Zhao, J.; Wang, B.T. Hexagonal M₂C₃ (M = As, Sb, and Bi) monolayers: New functional materials with desirable band gaps and ultrahigh carrier mobility. *J. Mater. Chem. C* **2018**, *6*, 12689–12697. [[CrossRef](#)]
26. Huang, L.F.; Gong, P.L.; Zeng, Z. Correlation between structure, phonon spectra, thermal expansion, and thermomechanics of single-layer MoS₂. *Phys. Rev. B* **2014**, *90*, 045409. [[CrossRef](#)]
27. Li, L.; Yu, Y.; Ye, G.J.; Ge, Q.; Ou, X.; Wu, H.; Feng, D.; Chen, X.H.; Zhang, Y. Black phosphorus field-effect transistors. *Nat. Nanotechnol.* **2014**, *9*, 372–377. [[CrossRef](#)]
28. Novoselov, K.S.; Jiang, D.; Schedin, F.; Booth, T.J.; Khotkevich, V.V.; Morozov, S.V.; Geim, A.K. Two-dimensional atomic crystals. *Proc. Natl. Acad. Sci. USA* **2005**, *102*, 10451–10453. [[CrossRef](#)]
29. Kara, A.; Enriquez, H.; Seitsonen, A.P.; Voon, L.L.Y.; Vizzini, S.; Aufray, B.; Oughaddou, H. A review on silicene—New candidate for electronics. *Surf. Sci. Rep.* **2012**, *67*, 1–18. [[CrossRef](#)]
30. Kresse, G.; Furthmüller, J. Efficient iterative schemes for ab initio total-energy calculations using a plane-wave basis set. *Phys. Rev. B* **1996**, *54*, 11169. [[CrossRef](#)]
31. Perdew, J.P.; Burke, K.; Ernzerhof, M. Generalized gradient approximation made simple. *Phys. Rev. Lett.* **1996**, *77*, 3865–3868. [[CrossRef](#)]
32. Blöchl, P.E. Projector augmented-wave method. *Phys. Rev. B* **1994**, *50*, 17953. [[CrossRef](#)]

33. Heyd, J.; Scuseria, G.E.; Ernzerhof, M. Hybrid functionals based on a screened Coulomb potential. *J. Chem. Phys.* **2003**, *118*, 8207–8215. [[CrossRef](#)]
34. Madsen, G.K.; Singh, D.J. BoltzTraP. A code for calculating band-structure dependent quantities. *Comput. Phys. Commun.* **2006**, *175*, 67–71. [[CrossRef](#)]
35. Xu, L.; Zheng, Y.; Zheng, J.C. Thermoelectric transport properties of PbTe under pressure. *Phys. Rev. B* **2010**, *82*, 195102. [[CrossRef](#)]
36. Zhu, X.L.; Liu, P.F.; Gao, H.; Xie, G.F.; Wang, B.T. Thermoelectric properties of hexagonal WN_6 from first-principles calculation. *ES Energy Environ.* **2018**, *3*, 80–87. [[CrossRef](#)]
37. Li, W.; Carrete, J.; Katcho, N.A.; Mingo, N. ShengBTE: A solver of the Boltzmann transport equation for phonons. *Comput. Phys. Commun.* **2014**, *185*, 1747–1758. [[CrossRef](#)]
38. Togo, A.; Tanaka, I. First principles phonon calculations in materials science. *Scr. Mater.* **2015**, *108*, 1–5. [[CrossRef](#)]
39. Li, W.; Lindsay, L.; Broido, D.A.; Stewart, D.A.; Mingo, N. Thermal conductivity of bulk and nanowire $Mg_2Si_xSn_{1-x}$ alloys from first principles. *Phys. Rev. B* **2012**, *86*, 174307. [[CrossRef](#)]
40. Pumera, M.; Sofer, Z. 2D monoelemental arsenene, antimonene, and bismuthene: Beyond black phosphorus. *Adv. Mater.* **2017**, *29*, 1605299. [[CrossRef](#)]
41. Peng, H.; Kioussis, N.; Snyder, G.J. Elemental tellurium as a chiral p-type thermoelectric material. *Phys. Rev. B* **2014**, *89*, 195206. [[CrossRef](#)]
42. Ding, G.; Wang, C.; Gao, G.; Yao, K.; Dun, C.; Feng, C.; Li, D.; Zhang, G. Engineering of charge carriers via a two-dimensional heterostructure to enhance the thermoelectric figure of merit. *Nanoscale* **2018**, *10*, 7077–7084. [[CrossRef](#)]
43. May, A.F.; Toberer, E.S.; Saramat, A.; Snyder, G.J. Characterization and Analysis of Thermoelectric Transport in n-type $Ba_8Ga_{16-x}Ge_{30+x}$. *Phys. Rev. B* **2009**, *80*, 125205. [[CrossRef](#)]
44. Singh, D.J. Electronic and thermoelectric properties of $CuCoO_2$: Density functional calculations. *Phys. Rev. B* **2007**, *76*, 085110. [[CrossRef](#)]
45. Parker, D.; Singh, D.J. Potential thermoelectric performance from optimization of hole-doped Bi_2Se_3 . *Phys. Rev. X* **2011**, *1*, 021005.
46. Yu, J.; Sun, Q. Bi_2O_2Se nanosheet: An excellent high-temperature n-type thermoelectric material. *Appl. Phys. Lett.* **2018**, *112*, 053901. [[CrossRef](#)]
47. Heremans, J.P.; Dresselhaus, M.S. 27 Low-Dimensional Thermoelectricity. *Acta Phys. Pol. A* **2005**, *108*, 609–634. [[CrossRef](#)]
48. Jonson, M.; Mahan, G.D. Mott's formula for the thermopower and the Wiedemann-Franz law. *Phys. Rev. B* **1980**, *21*, 4223. [[CrossRef](#)]
49. Nika, D.L.; Pokatilov, E.P.; Askerov, A.S.; Balandin, A.A. Phonon thermal conduction in graphene: Role of Umklapp and edge roughness scattering. *Phys. Rev. B* **2009**, *79*, 155413. [[CrossRef](#)]
50. Liu, P.F.; Bo, T.; Xu, J.; Yin, W.; Zhang, J.; Wang, F.; Erillsson, O.; Wang, B.T. First-principles calculations of the ultralow thermal conductivity in two-dimensional group-IV selenides. *Phys. Rev. B* **2018**, *98*, 235426. [[CrossRef](#)]
51. Xie, G.F.; Ding, D.; Zhang, G. Phonon coherence and its effect on thermal conductivity of nanostructures. *Adv. Phys. X* **2018**, *3*, 1480417. [[CrossRef](#)]
52. Qin, G.; Qin, Z.; Fang, W.Z.; Zhang, L.C.; Yue, S.Y.; Yan, Q.B.; Hu, M.; Su, G. Diverse anisotropy of phonon transport in two-dimensional group IV–VI compounds: A comparative study. *Nanoscale* **2016**, *8*, 11306–11319. [[CrossRef](#)]
53. Bardeen, J.; Shockley, W. Deformation potentials and mobilities in non-polar crystals. *Phys. Rev.* **1950**, *80*, 72–80. [[CrossRef](#)]
54. Harman, T.C.; Taylor, P.J.; Walsh, M.P.; LaForge, B.E. Quantum dot superlattice thermoelectric materials and devices. *Science* **2002**, *297*, 2229–2232. [[CrossRef](#)]

